Universiteit Utrecht

ALICE

Physics and Astronomy

Improving the neutral meson raw yield extraction in ALICE

Bachelor Thesis

Remco van Horik

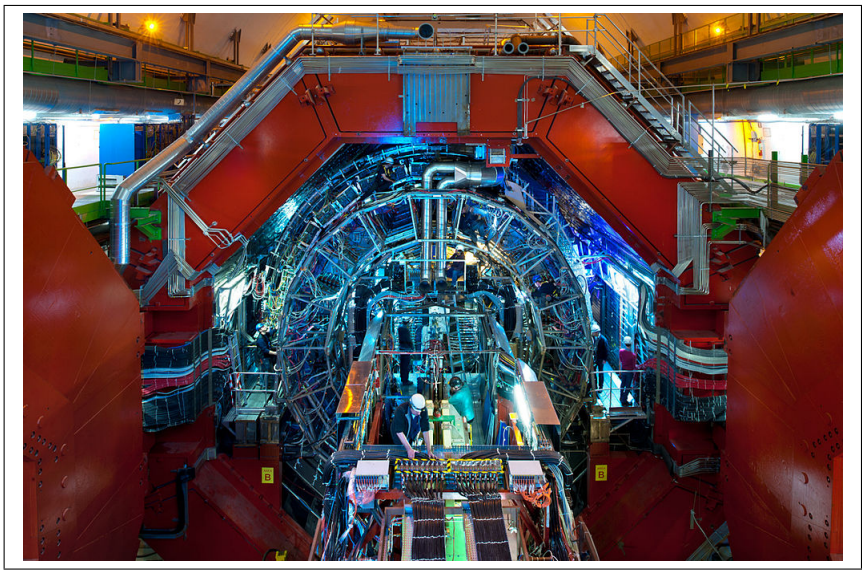

Supervisors:

Prof. Dr. T. Peitzmann
Institute for Subatomic Physics, University Utrecht

Msc. M.H.P.A. Sas
Institute for Subatomic Physics, University Utrecht

June 13, 2018

Abstract

In this bachelor thesis a new method of extracting the raw yield for neutral mesons (π^0, η) in ALICE is introduced. The measurement is done by the Electromagnetic Calorimeter of the ALICE detector in p-Pb collisions. The data from this measurement is used to create invariant mass distributions. Each of these mass distributions are fitted with a Gaussian function for their p_T-bin. The parameters μ, σ (and λ for π^0) from these Gaussians are fitted with polynomial functions to describe them as a function of p_T. Due to this constraint the fluctuations of these parameters around the binpoints become less. This gives a new extracted signal. Now instead of numerical integrating the background subtracted signal this thesis will use an analytical, continuous integration from $\mu\pm$ 2σ, 3σ and 4σ to extract the raw yield. So there are two new raw yields, those that are integrated with and those without constraint. The values per binpoint are comparable to the values of the numerical yield, so both methods can be used. In the end the analytical raw yields combined with the numerical yields give a more realistic view at the deviation and the RMS value, since other methods are used to calculate the raw yield.

Picture front page:
This is the ALICE detector, which is one of the four large detectors at CERN [1]. The picture is taken by Antonio Saba on 01/02/2012 and gives a general overview of the detector[2].

Contents

1 Introduction

In this section a general introduction into elementary particles and heavy ion collisions is given. Also the derivation for the used invariant mass equation is given.

1.1 Early Universe

Around 13.77 billion years ago the universe rapidly expanded into existence [3]. When it was just a millionth of a second old it was filled with a hot, dense soup consisting of quarks (fundamental particles) and gluons (strong force carriers). Normally the quarks are *confined*, which means they are bound with other quarks and cannot move freely on its own in nature. However, when recreating these extreme conditions, a phase transition occurs leading to deconfinement and the so-called Quark-Gluon Plasma (QGP) , where quarks and gluons can move freely in a plasma (hence the name) [4]. This is the state in which the universe was, before it expanded further and confinement did take place (leading to the creation of all the matter we know today). The recreation of the QGP happens in powerfull accelerators that make head-on collisions between massive ions, like lead ions. This thesis will use the data from the ALICE experiment of the Large Hadron Collider (LHC) in CERN, where such collisions are recreated. In these collisions nuclei collide and create a very small fireball in which everything "melts" into a QGP. When the fireball cools down and expands the individual quarks and gluons recombine into ordinary matter, creating the hadron gas. Between the QGP and hadron gas phase is a mixed phase in which the hadron gas is still forming and the QGP decreases. The particles in the hadron gas decay very quickly in new particles such as mesons, baryons and leptons, which then can be detected [5]. Mesons and baryons consist of confined quarks. The quarks and leptons together form most of the particles in the standard model, which are shown in figure 1.

The space time evolution of the collision can be seen in figure 2.

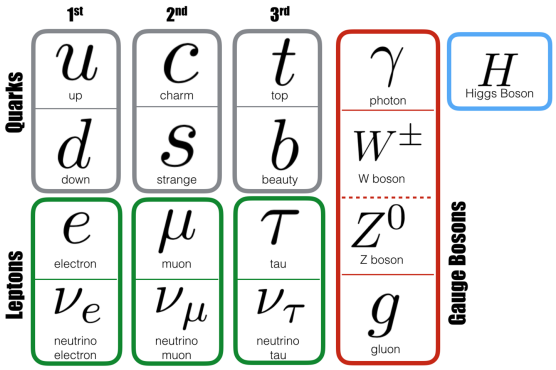

Figure 1: The particles in the standard model. All particles are considered to be the building blocks of our modern universe.

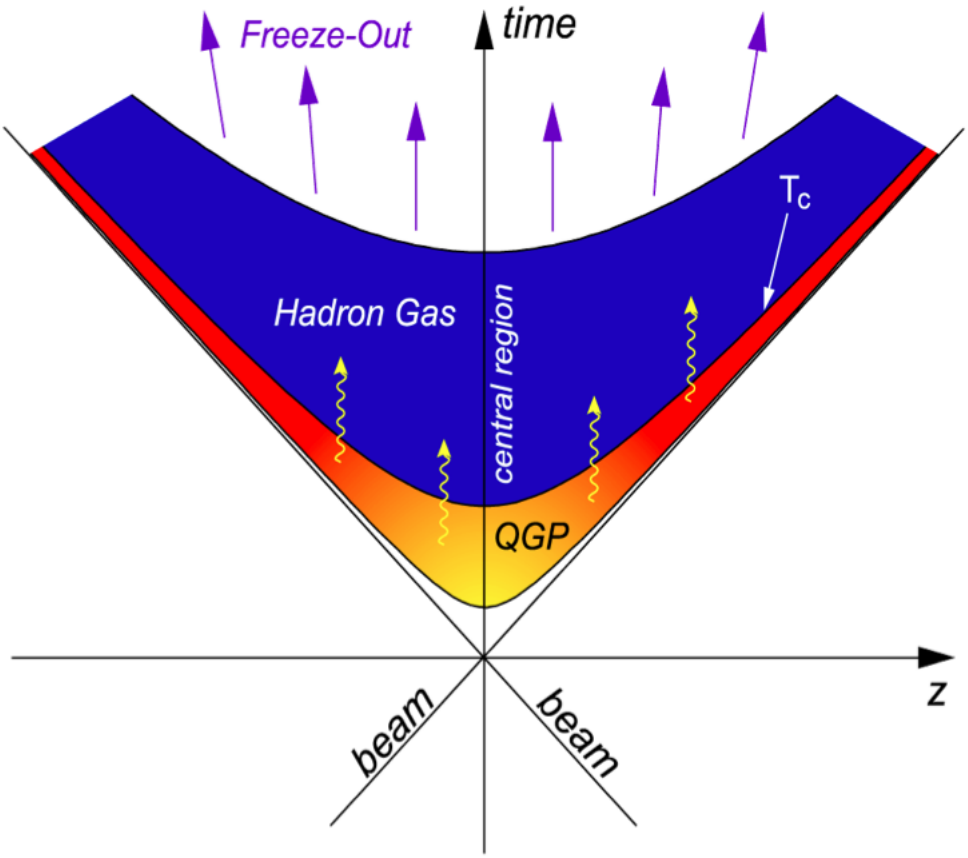

Figure 2: The space-time evolution of heavy ion collisions

When the LHC recreates these collisions the ALICE detector measures the reaction products, i.e., hadrons, leptons, photons (light particles) and gluons, in the form of electric signals. By measuring the direct photons, γ's, the temperature of the QGP is derived. Sadly enough not all photons come directly from the QGP, but some are the decay products from other particles such as neutral mesons, π^0 and η, which decay most of times in two photons. These decay photons form a background in extracting direct photons. These mesons are the combination of a quark and anti-quark, for π^0 the quark content is $\frac{u\bar{u}-d\bar{d}}{\sqrt{2}}$ and for η it is $\frac{u\bar{u}+d\bar{d}+2s\bar{s}}{\sqrt{6}}$.

1.2 Invariant mass

To know which photons came directly from the QGP and which from the neutral mesons a raw yield of the mesons must be reconstructed. Luckily the mass of the mesons stays invariant, even though they decayed into two photons. Then by using four dimensional vectors (so called four-momentum vectors) and relativity the invariant mass can be calculated. The mother particle, π^0 or η, is at rest in its own rest frame, so it has momentum $\vec{p}^{\mu} = \begin{pmatrix} M \\ \vec{0} \end{pmatrix}$ in natural units, where M is the rest mass of the meson. The decay particles, the two photons, are moving with momenta $|\vec{p}_1^{\mu}| = E_1$ and $|\vec{p}_2^{\mu}| = E_2$.The

invariant mass can be calculated as:

$$\vec{p}_\mu \cdot \vec{p}^\mu = (\vec{p}_1 + \vec{p}_2)_\mu \cdot (\vec{p}_1 + \vec{p}_2)^\mu$$
$$M^2 = 2E_1E_2 - 2E_1E_2\cos(\theta_{12})$$

$$M_{\gamma\gamma} = \sqrt{2E_1E_2(1 - \cos(\theta_{12}))}, \tag{1}$$

with θ_{12} the opening angle between the photons, where the angle is calculated in the lab frame. Random pairs lead to an arbitrary value of the mass, but pairs that do originate from a given meson decay will be observed as a peak around the true mass. This peak has a certain finite width due to detector resolution. The invariant masses of π^0 and η are, respectively, 0.135 GeV/c^2 and 0.548 GeV/c^2. More information about the invariant mass and their mass distributions will be presented in section 3.2.

This thesis will provide a new method of extracting the raw yield of the neutral mesons and quantify what effect this has in comparison with the currently used method. Also a new way to create different mass distribution fits by fitting their parameters will be introduced.
By reconstructing the neutral mesons a small but significant step towards assessing the early stages of the universe is performed.

2 The ALICE detector

ALICE (A Large Ion Collider Experiment) is a detector at the Large Hadron Collider (LHC) ring of CERN and is specialized to study, as the name suggests, heavy-ion (Pb-Pb) collisions. It is approximately 16 meters high, 16 meters wide, 26 meters long and weighs about 10,000 tons. The LHC provides collisions between lead ion, creating the QGP. As ALICE receives the beams from the LHC it observes the particles created in the QGP as the plasma expands and cools [7]. ALICE consists of 19 different subdetectors (which can

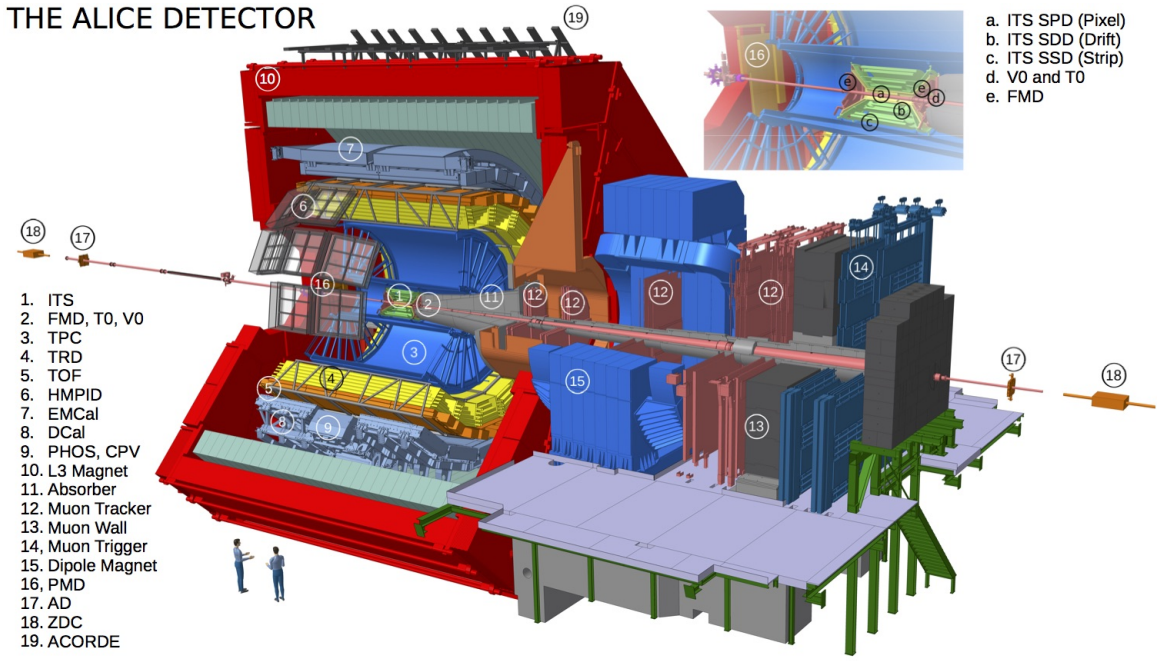

Figure 3: An overview of the ALICE detector

be seen in figure 3) that use different techniques to identify and get information from the particles produced in the collisions which take place at its centre, so that the evolution of the system produced during these collisions can be reconstructed and studied [8]. The most important subdetectors for this thesis will be described briefly.

2.1 Inner Tracking System

The Inner Tracking System (ITS) of the ALICE experiment consists of six layers of silicon detectors exploiting three different technologies: pixel (SPD), drift (SDD) and strip (SSD), which are shown in figure 4. The main tasks of the ITS are to reconstruct the primary and secondary vertices, to track and identify *charged* particles with a low p_T cutoff, and to improve the momentum resolution at high p_T [9].

2.2 Time Projection Chamber

Around the ITS the Time Projection Chamber is placed, which can be seen in figure 5. This is a 90 m^3 cylinder filled with a gas which is ionised when charged particles interact with it. The charged particle then loses energy through the ionisation of the atoms [10]. The liberated electrons from this ionisation drift toward the endplates of the cylinder by an applied electric field. The signals read out by the paths of the chamber provide 3

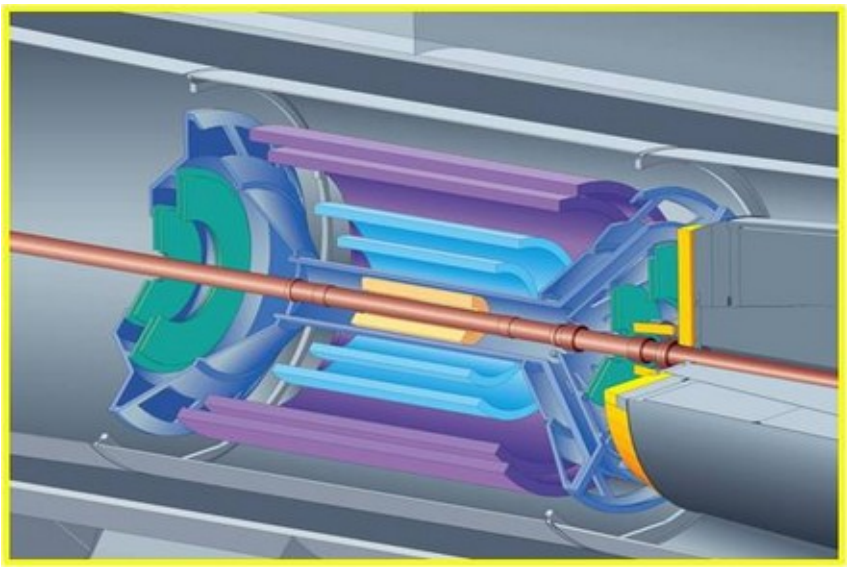

Figure 4: The ALICE Inner Tracking System. The three different layers of silicon detectors SPD, SDD and SSD are shown respectively in yellow, blue and purple.

dimensional information of the trajectory of the particles and measure their energy loss [11].

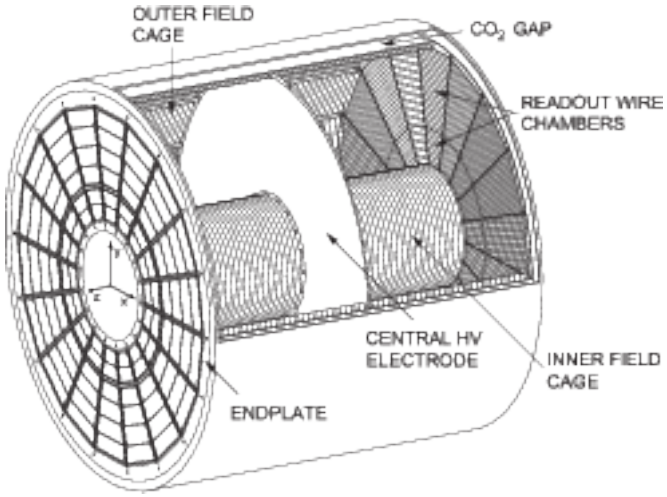

Figure 5: The ALICE Time Projection Chamber

2.3 Electromagnetic calorimeter

The EMCal is an electromagnetic calorimeter with a large acceptance (110 degrees azimuthal, from -0.7 to 0.7 on pseudorapidity) and weighs about 100 tons. It can trigger and reconstruct high energy γ's, $e^{\pm}$'s and jets in ALICE. The EMCal enables a study of jet interactions in the medium produced in heavy ion collisions at the LHC. The structural units are the EMCal Super Modules. Each Super Module is assembled from 96 modules, which are single self-contained detector units. A particle passing through the module and interacting with the lead produces an electromagnetic shower, which produces light

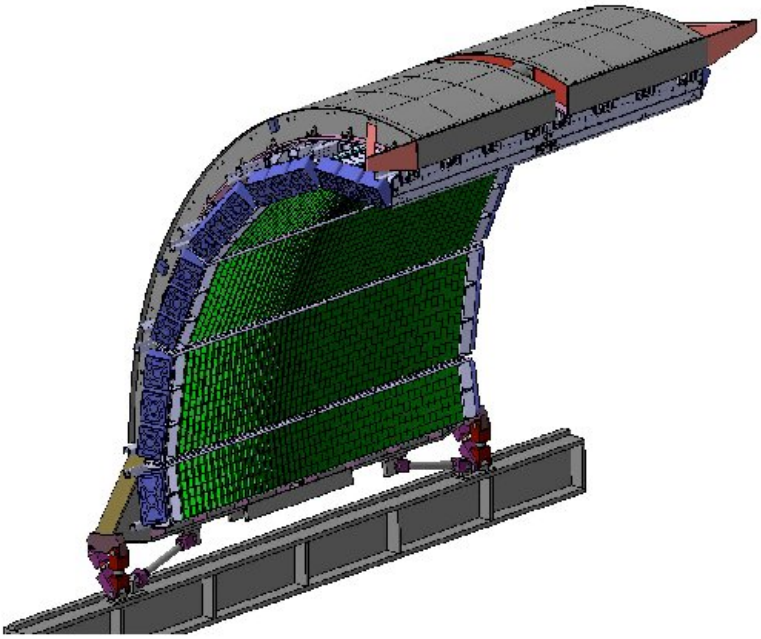

Figure 6: The ALICE Electromagnetic Calorimeter.

(photons) in the plastic scintillators. These photons are converted into an electric signal with an amplitude proportional to the energy of the original incoming particle [12].

3 Yield extraction

This section describes the method of reconstructing photons and neutral mesons, π^0 and η, and how the raw yield is extracted with the currently used method.

3.1 Photon reconstruction with the EMCal

As written in [13]: The ALICE detector can reconstruct photons using many different techniques. The calorimetric method has its strength at higher energies and can reconstruct photons with E > 500 MeV while having high reconstruction efficiency and acceptance. In this thesis the calorimetric method using the EMCal is used for the neutral meson analysis. Photons that hit a calorimeter create many secondary particles via processes such as Bremsstrahlung and pair production. This is called an electromagnetic shower, which spreads in longitudinal and transverse direction. In order to reconstruct the energy of the particles we have to use clusterizer algorithms which find adjacent cells and sum up their energies. To reconstruct the clusters the algorithm V2 is used.
To characterize the shape of the found clusters, the shower shape parameters M02 and M20 are also used. These moments are calculated in general by:

$$M_{mn} = \sum_k (x^{(k)})^m (y^{(k)})^n E_k;\ m, n = 0, 1, 2... \tag{2}$$

Here k runs over all cells in the cluster, x and y are the cell coordinates in the cluster coordinate system and E_k is the cell energy. The total energy of the cluster is the sum of the energies of the cells belonging to the cluster. The new cluster energy correction is applied on MC with the purpose of matching the MC cluster energies to data cluster energies. The energy of the cluster is calculated from the p_T of the meson, since only photons of similar energies are paired for the EMCal-EMCal method. This constraint is applied by a cut in the energy asymmetry of the photon pair. The EMCal-EMCal cluster energy correction will be used in the determination of the systematic uncertainty. For the PCM-EMCal the energy of the conversion photon is known and the EMCal photon is not constrained. The first set of cuts are applied on cell level, the second on cluster level. To remove charged clusters, clusters are rejected if a charged track is pointing to the clusters. The charged track is reconstructed using the TPC and extrapolated to the EMCal surface. The applied cuts are kept loose so that most photon-like candidates are accepted. This is appropriate for neutral meson analyses, which is explained in a later chapter [14].

3.2 Neutral meson reconstruction

3.2.1 Invariant mass

Since both neutral mesons most of the time decay into the same particles, namely $\gamma\gamma$, the same method can be applied to reconstruct these mesons. The photons are obtained using the clusterizer algorithms. The additional selection is done using the EMCal cell and cluster cuts. As described in section 1.2 the invariant mass is given by equation (1). For π^0 the invariant rest mass is 0.135 GeV/c^2 and for η 0.548 GeV/c^2. Since each photon combination counts as one, there will be a peak around the invariant mass of the meson. An example of such an invariant mass distribution can be seen in figure 7.

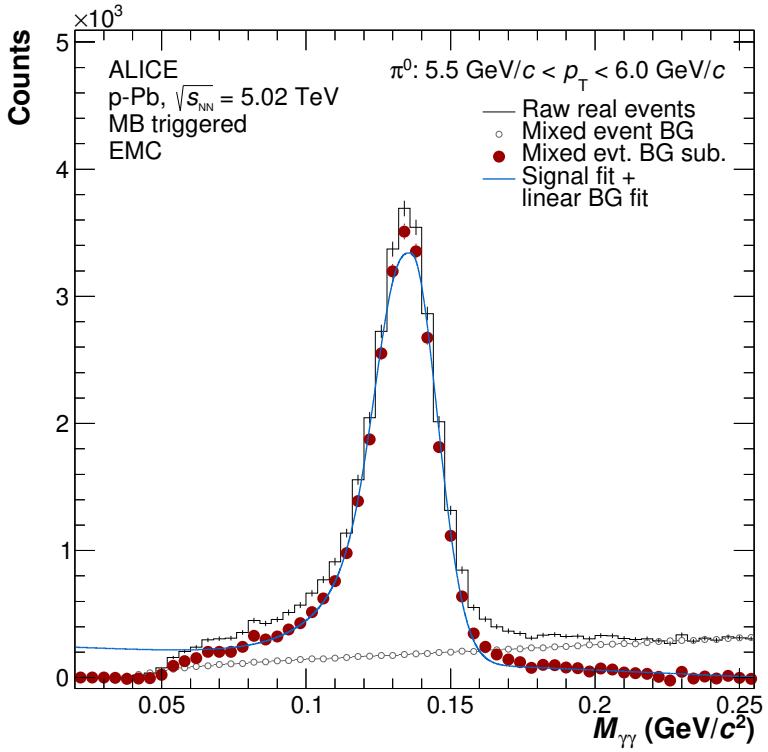

Figure 7: An example of an invariant mass distribution for π^0. The black line is the number of counts of the corresponding mass at that point. The white dots represent the Event Mixing background. The blue line is the fit through the background subtracted numerical integrated signal, which is referred to with red dots.

In section 4 can be seen that the invariant mass plots for π^0 have high peaks around its invariant mass, even when the background is not substracted. For η the invariant mass becomes clearer when the background signal is substracted. Since η is less visible than π^0 and η has a larger width, the extraction of the η meson is much harder.
The background is calculated with the Event Mixing technique, which destroys the correlations of photon pairs by combining photons from different events. The shape of the background depends on the multiplicity of the event and the primary vertex position [15].

3.2.2 Signal extraction

The invariant masses, obtained from equation (1), are used to extract the signal. The combinatorial background from the Event Mixing technique is scaled to match the background of the combined signal and background distribution. The invariant mass minus the combinatorial background distribution is fitted with:

$$y = A(G(M_{\gamma\gamma}) + e^{\frac{(M_{\gamma\gamma}-\mu)}{\lambda}}(1 - G(M_{\gamma\gamma}))\theta(M_{\gamma\gamma} - \mu)) + B + C \cdot M_{\gamma\gamma}, \tag{3}$$

$$\text{with } G(M_{\gamma\gamma}) = e^{-0.5(\frac{(M_{\gamma\gamma}-\mu)}{\sigma})^2}. \tag{4}$$

Here G($M_{\gamma\gamma}$) is a Gaussian with width σ and mean μ of the corresponding meson. The inverse slope of the exponential function is represented by λ. The linear component B+C$\cdot M_{\gamma\gamma}$ is added in case the combinatorial background does not fully describe the background shape of the signal. B and C correspond to the startvalue and slope of the linear component, respectively. The θ-function is the Heavyside-function which switches the contribution of the exponential function on or off. In section 4.1 will be explained how these parameters are used to develop a new method to extract the raw yield. An example of a fit through a background subtracted invariant mass can also be seen in figure 7.
To extract the meson raw yields, the background substracted invariant mass distributions are numerically integrated around the fitted peak position of the meson. This is done by:

$$N^{\pi^0}_{raw} = \int_{M^0_\pi - 0.032GeV/c^2}^{M^0_\pi + 0.022GeV/c^2} (N^{\gamma\gamma} - N^{comb.BG})dM_{\gamma\gamma} - \int_{M^0_\pi - 0.032GeV/c^2}^{M^0_\pi + 0.022GeV/c^2} (B + C \cdot M_{\gamma\gamma})dM_{\gamma\gamma}. \tag{5}$$

This is the standard integration range for π^0. For η it is (M_η - 0.060 GeV/c^2, M_η + 0.050 GeV/c^2) due to the fact that its peaks are wider [13]. These standard integration ranges can differ with a maximal and minimal value from the standard integration. The most wide and narrow integration ranges (of which the exact values are not included in this thesis) are be called "maximal positive" and "maximal negative", respectively and will be referred to in a later section. This is due to the fact that the statistical error will be positive and negative for the wide and narrow ranges. Later on there will also be presented a new way to extract the raw yield.

4 Results

4.1 Neutral meson parameters

In the following subsection the method and results for the new parameter values are explained and shown.
For each p_T bin the invariant mass is calculated. As described in the previous section, every parameter come from the fitted Gaussian invariant masses, which means the parameters are p_T dependent. The amplitude, mean, sigma (width), lambda and the linear components (startvalue and slope) are all included in those fits. After getting these datapoints for π^0 and η the mean μ and sigma σ are fitted with the polynomial functions

$$\mu_{\pi^0,\eta} = f_0 + f_1 \cdot p_T + f_2 \cdot p_T^2 + f_3 \cdot p_T^3, \tag{6}$$

$$\sigma_{\pi^0} = g_0 + g_1 \cdot p_T + g_2 \cdot p_T^2 + g_3 \cdot p_T^3 + g_4 \cdot p_T^4, \tag{7}$$

$$\sigma_{\eta} = h_0 + h_1 \cdot p_T^{-1} + h_2 \cdot p_T^2, \tag{8}$$

where $f_{0,1,2,3}$, $g_{0,1,2,3,4}$ and $h_{0,1,2}$ are the best chosen parameters through the datapoints and p_T is the transverse momentum. The results of π^0 and η are shown respectively in figure 8 and 9. These fits don't work for the amplitude, startvalue and slope since their binsize are rescaled. Each time the values get too small the binsize increases so more bins can be counted. The lambdatail is fitted for only the π^0 particles with the function $j_0 + j_1 \cdot p_T + j_2 \cdot p_T^{-2}$, since its value for η is fixed at 0.033. This significance is not very large, since contribution of lambda to the Gaussian is much less than the weights of mean and sigma. This can also be seen in equation (3).
The main reason to constrain these parameters with the polynomial fits is that the fluctuations of the parameters become much smaller, since the values of the fits at their p_T will later be evaluated instead of the points themself.
These new parameter values from the fitted functions are plugged in equation (3). This means there are two Gaussians for the same data, the first one is described in the previous section and the second one uses the parameter fits evaluated at the same p_T-values to create new Gaussians. These are shown in figures 20 for π^0 and 21 for η in appendix A. In figure 8 can be seen that the polynomial functions fit well through the datapoints for π^0 and therefore one should not expect many surprising differences in the fits for the mass distributions. This is exactly the case in figure 10 and 11, for both low and high p_T values. As for η, in figures 12 and 13 there are some differences. First of all, the shape of the graph is different. The constrained fit at low p_T is wider than the unconstrained fit, while the opposite is true for high p_T values. This is in line with the values of σ and its constrained fit, which has a higher value than the datapoint itself at the second p_T value. Therefore the constrained fit is wider than the unconstrained one. For the last value, the opposite is true. The fit is lower than the datapoint, which means the peak for the unconstrained fit is wider. The fact that η differs more from the unconstrained fit than π^0 does, was expected, since the extraction for η is harder, which was earlier stated in section 3.2.1.

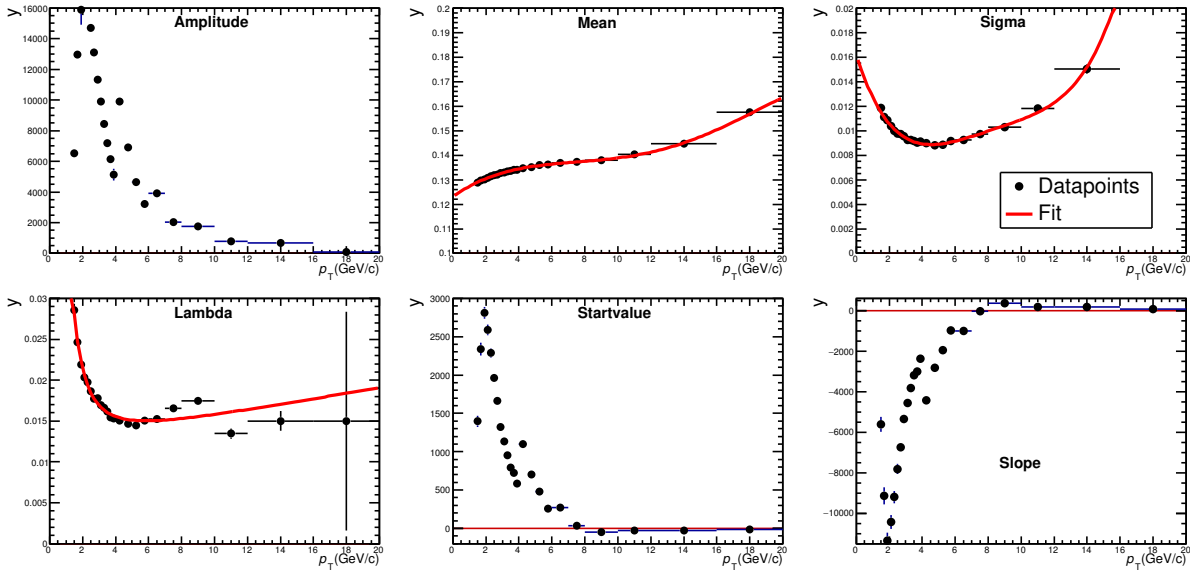

Figure 8: The datapoints for the amplitude, mean, sigma, lambda and linear components (startvalue, slope) for π^0. The mean, sigma and lambdatail are fitted with polynomial functions.

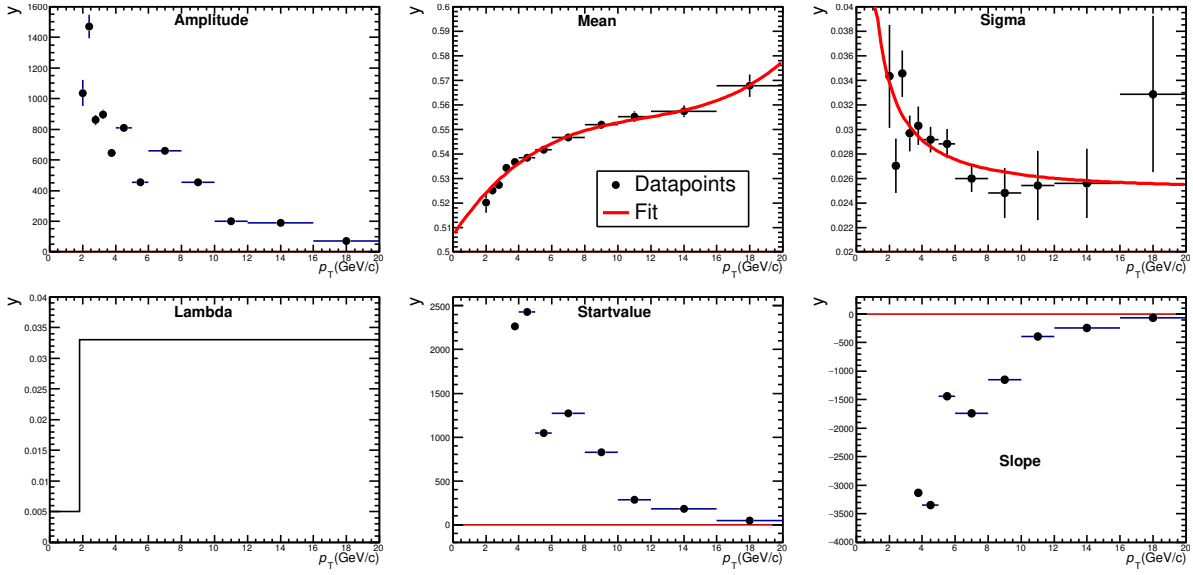

Figure 9: The datapoints for the amplitude, mean, sigma, lambda and linear components (startvalue, slope) for η. The mean and sigma are fitted with polynomial functions.

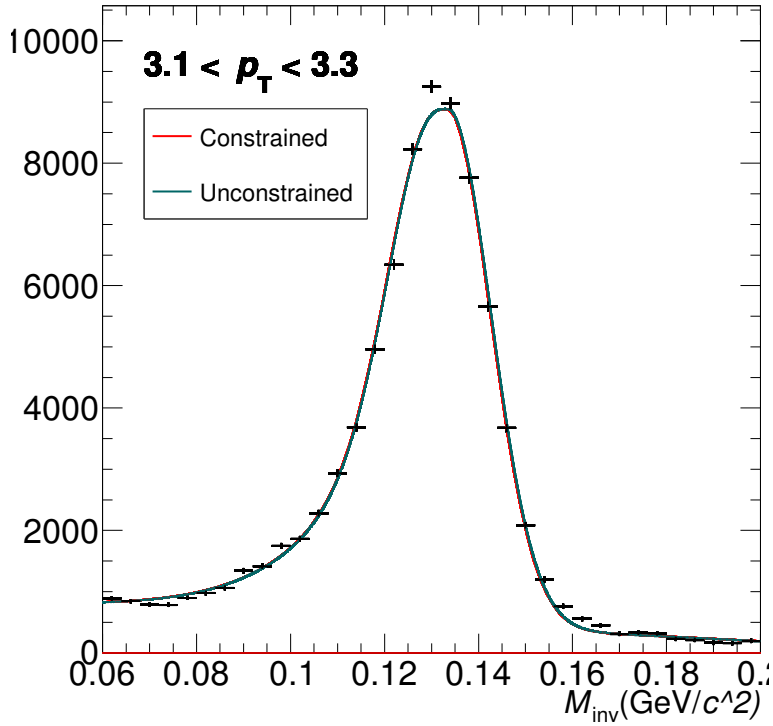

Figure 10: The invariant mass distribution fits of π^0 for $3.1 < p_{\mathrm{T}} < 3.3$.

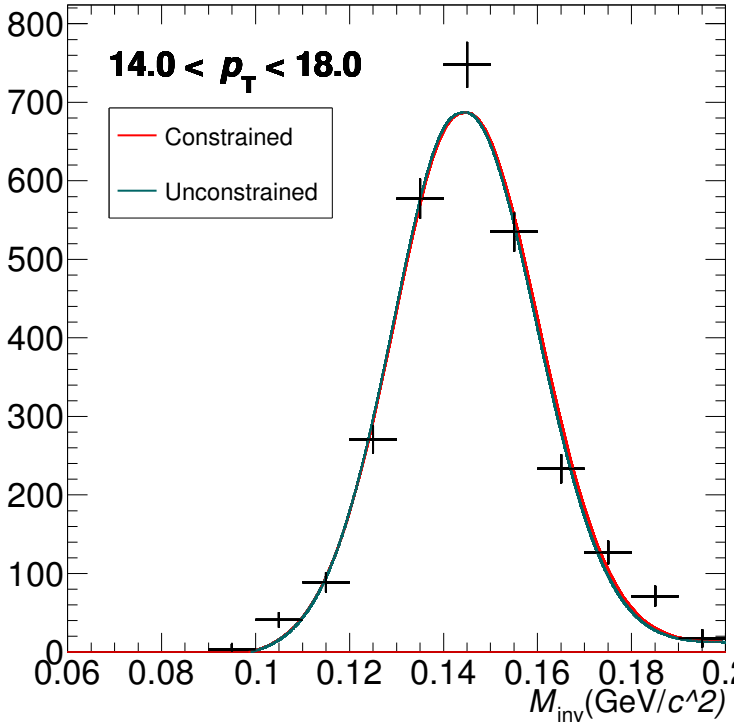

Figure 11: The invariant mass distribution fits of π^0 for $3.1 < p_{\mathrm{T}} < 3.3$.

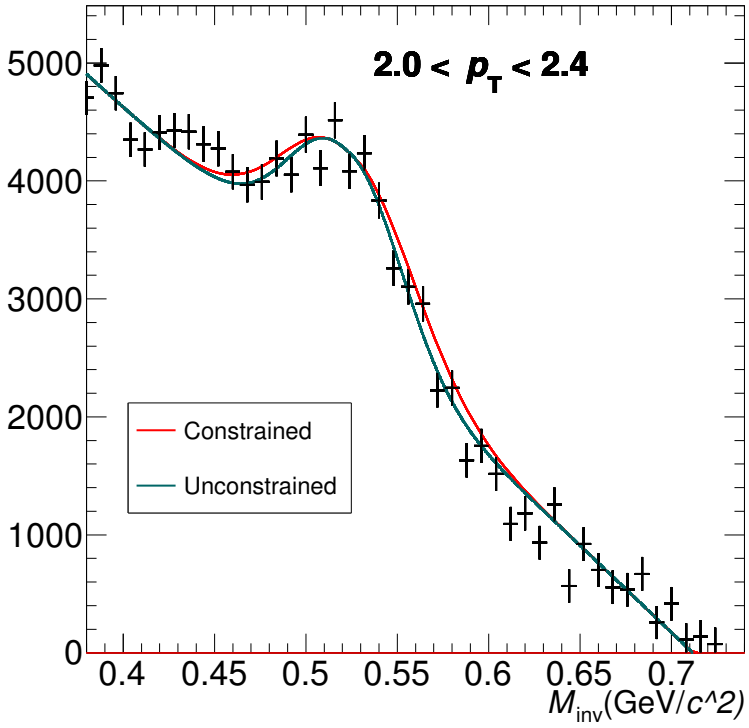

Figure 12: The invariant mass distribution fits of η for $9.0 < p_T < 11.0$.

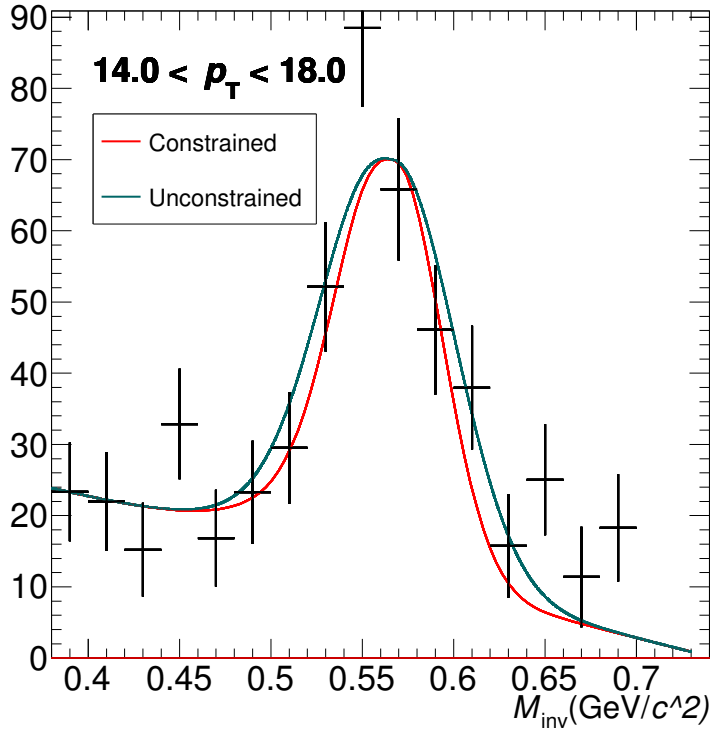

Figure 13: The invariant mass distribution fits of η for $14.0 < p_T < 18.0$.

4.2 Neutral meson raw yield extraction

Thus far the parameterfits created new Gaussians. In this subection the results of these Gaussians will be brought up to see what effect they have on the raw yield. This section will also introduce the new way of calculating the raw yield.

4.2.1 Integrated yield

Section 3.2.2 shows the current way of extracting the raw yield by numerical integrating the mass distributions around their peak. Now instead of doing this numerical this thesis will use analytical, continuous integration. In order to do this, one must subtract the background signal from the original data. Then the integration is done by:

$$N_{raw}^{\pi^0,\eta} = \int_{\mu-(2\sigma,3\sigma,4\sigma)}^{\mu+(2\sigma,3\sigma,4\sigma)} G - \int_{\mu-(2\sigma,3\sigma,4\sigma)}^{\mu+(2\sigma,3\sigma,4\sigma)} (B + C \cdot M_{\gamma\gamma}), \tag{9}$$

where B and C together with the Gaussian function G (with and without the constraint of the parameter fit) are described in equation (3) . The boundaries are $\mu\pm$ 2σ, 3σ and 4σ. This means there are six new values: three for the Gaussians with the parameterfit and three for the Gaussians without. In figure 14 and 15 the ratio between the obtained raw yield and the numerical yield is shown. If the raw yield would be perfect, then the ratio would be one, since there would be no difference between the numerical and the calculated yield. The deviation in the raw yield ratio is calculated by:

$$\sigma_R = R \cdot \sqrt{\left(\frac{\sigma_N}{N_{raw}^{\pi^0,\eta}}\right)^2} = R \cdot \sqrt{\frac{1}{N_{raw}^{\pi^0,\eta}}}. \tag{10}$$

Here R is the raw yield ratio, N the integrated raw yield. Due to the fact that $\sigma_N = \sqrt{N}$ and because the numerical integrated signal is correlated to the analytical yield, one gets equation (10).
In figure 14 and 15 the ratio between the obtained raw yield and the numerical yield is shown. If the raw yield would be perfect, then the ratio would be one, since there would be no difference between the numerical and the analytical yield. Since 2σ does not cover the entire Gaussian (95 percent) and the difference between 3σ and 4σ is neglectible (99.7 percent to 99.9), the only used ratio to determine the deviation and the RMS, explained in the following section, is the 3σ ratio.
Now that the ratio's of the analytic integration are known, they can be compared to the values of the ratio's calculated with numerical integration. The deviation of the analytically integrated yields are calculated by their difference with respect to the numerical ratio with standard boundaries. For example: when the difference between the (un)constrained ratio and the numerical ratio (which is always at y=1) is 0.02, the deviation is 2 percent. These results are plotted in figure 16 for π^0 and 17 for η. The light and dark blue line correspond to deviation of the maximum negative and positive integration, earlier mentioned in section 3.2.2. These are also calculated with respect to the numerical integration with standard boundaries. The values of the analytical integration have mostly the same form as the values for the negative numerical integration. This makes sense, because the ratio's are most of the time below y=1.

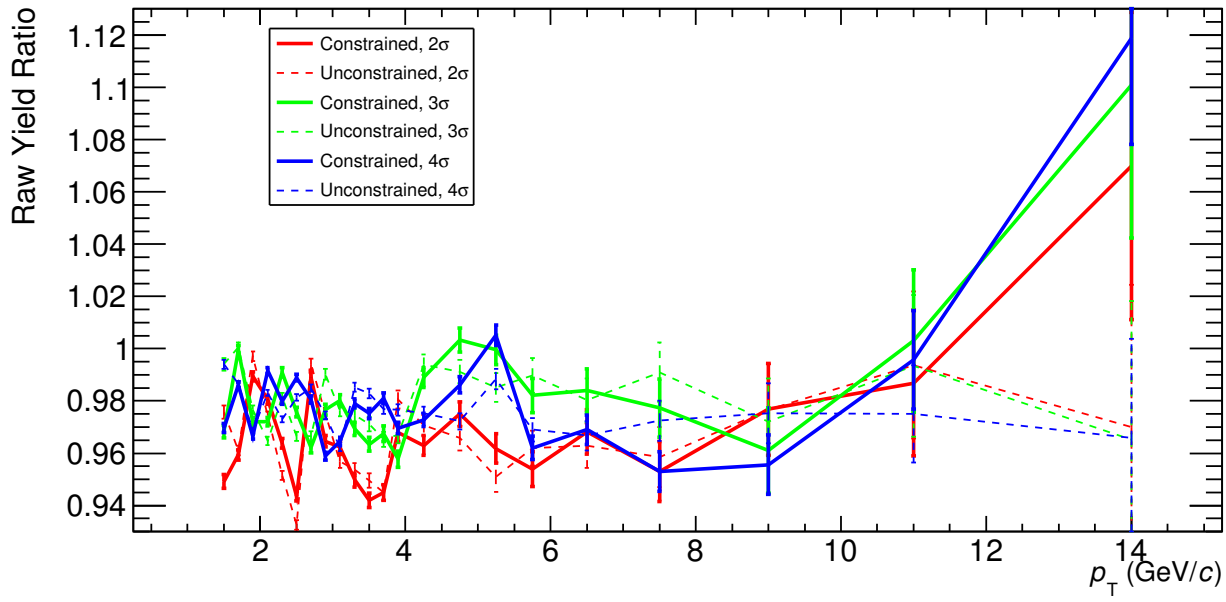

Figure 14: The ratio's between the calculated raw yield and the numerical yield per p_T bin for each integration boundary for π^0. The dotted lines correspond to the integrated Gaussians without constrained parameters and the normal lines to the Gaussians with the constrained parameterfit.

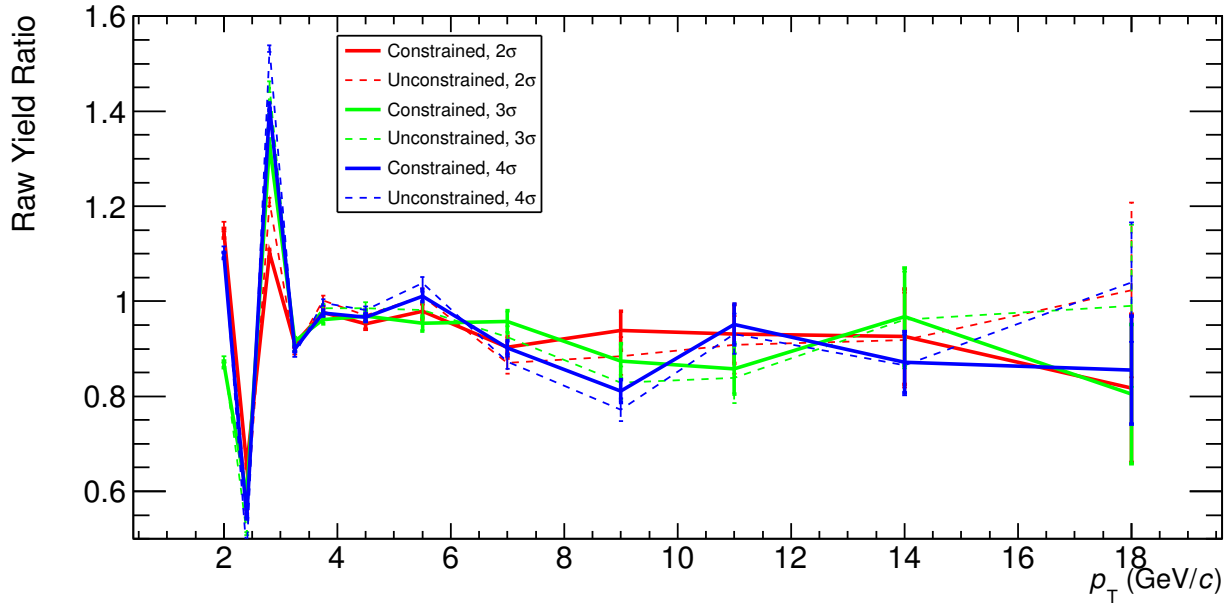

Figure 15: The ratio's between the calculated raw yield and the numerical yield per p_T bin for each integration boundary for η. The dotted lines correspond to the integrated Gaussians without constrained parameters and the normal lines to the Gaussians with the constrained parameterfit.

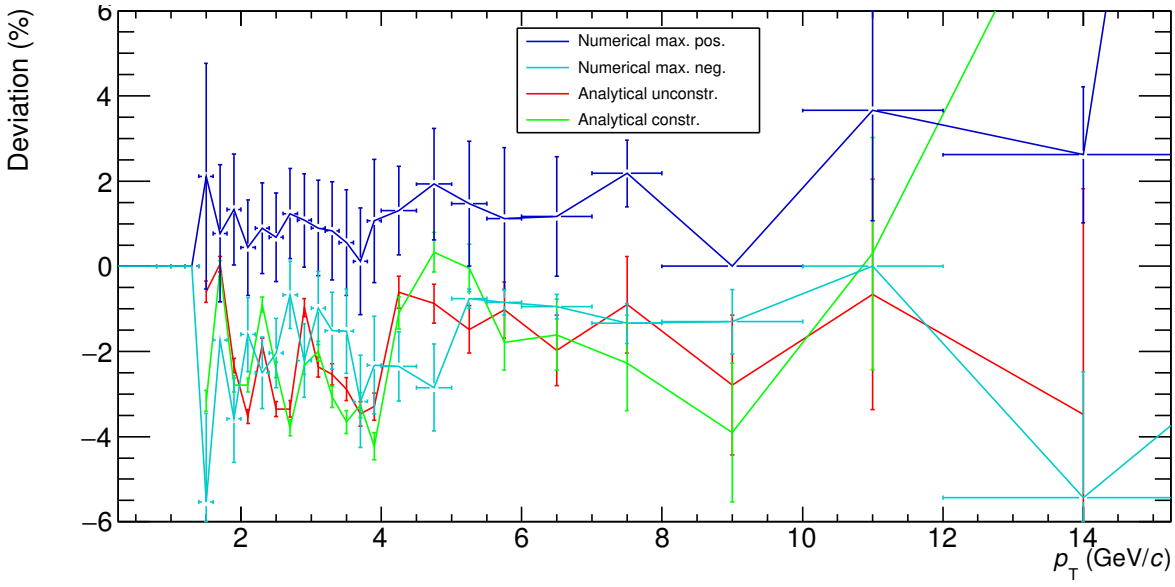

Figure 16: The deviation of the raw yields ratio's for π^0. The dark blue line and light blue line correspond to the maximal positive and maximal negative numerical integrated raw yield. The green and red lines are the analytically integrated raw yields with and without constraint, respectively.

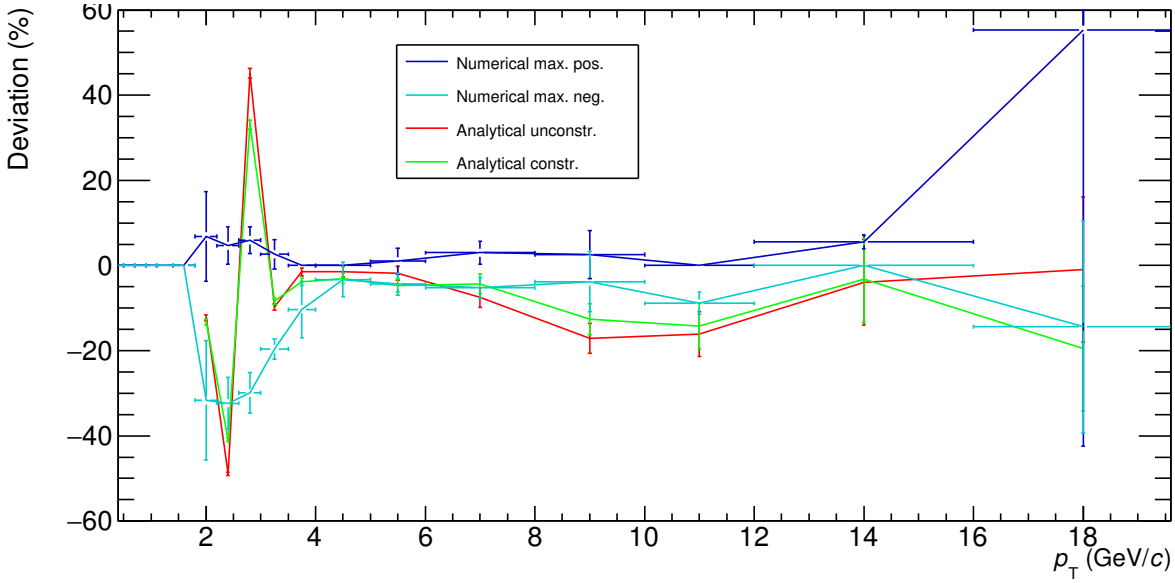

Figure 17: The deviation of the raw yields ratio's for η. The dark blue line and light blue line correspond to the maximal positive and maximal negative numerical integrated raw yield. The green and red lines are the analytically integrated raw yields with and without constraint, respectively.

4.2.2 Root Mean Square

In order to find the quadratic mean from the signal the Root Mean Square (RMS) is calculated. This is used to calculate out how far on average the deviation is from 0 [16]. The four methods, two numerical (positive and negative) and two analytical (constrained and unconstrained) integrated yields, result in two RMS values. The first one consists of only the RMS values with the two numerical yields. The second one consists of all four methods. The RMS values are determined by

$$\mathrm{RMS}_{\mathrm{Num}} = \sqrt{\frac{B_{Pos.}^2 + B_{Neg.}^2}{2}}, \tag{11}$$

$$\mathrm{RMS}_{\mathrm{Tot}} = \sqrt{\frac{B_{Pos.}^2 + B_{Neg.}^2 + A_{const.}^2 + A_{unconst.}^2}{4}}, \tag{12}$$

with B the numerical and A the analytical integrated yield. Figure 18 shows the RMS-values for π^0 at every binpoint and figure 19 for η. The lines are quite close to each other and have the same form, which means there is no unusual result. The new values include another systematic check so they should be more reliable. They agree with the old values, so they confirm the earlier error estimates.

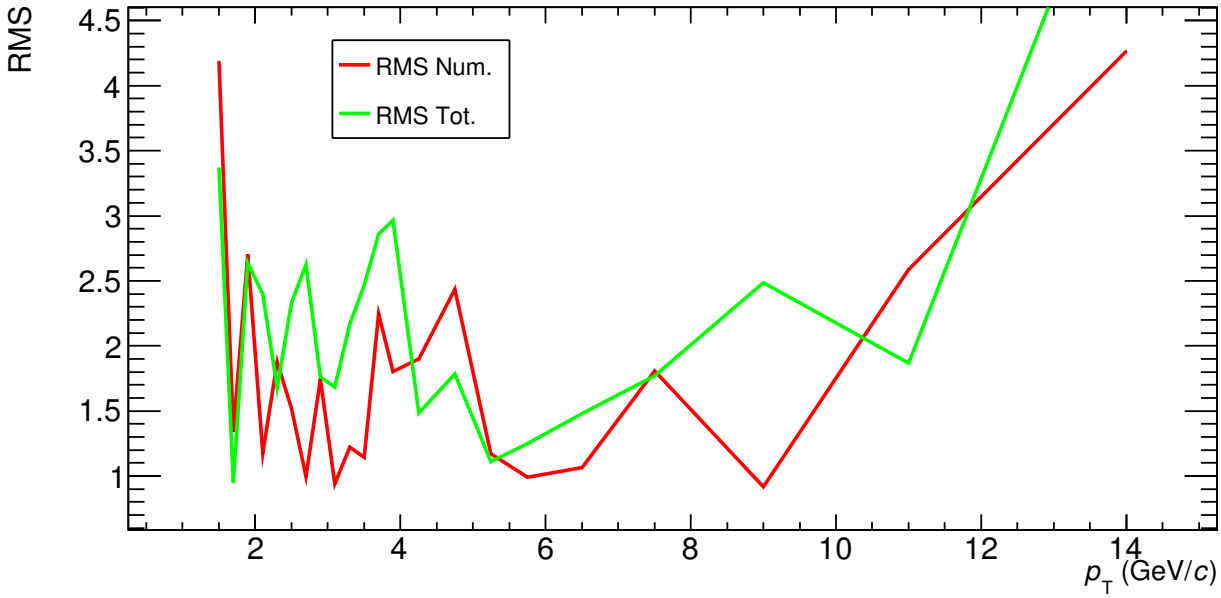

Figure 18: The RMS values for π^0 at every p_T value. The red line represents the RMS of the bincounted raw yield and the green line includes the new integrated yields.

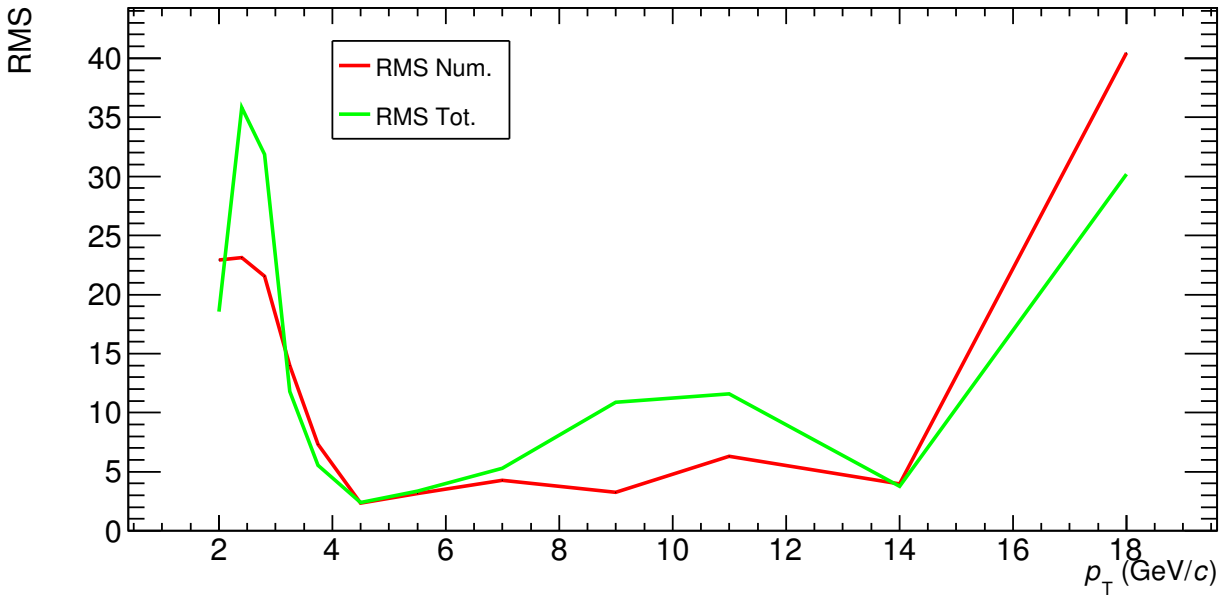

Figure 19: The RMS values for η at every p_{T} value. The red line represents the RMS of the numerical integrated raw yields and the green line includes the analytical integrated yields.

5 Conclusion, discussion and outlook

The early stage of the universe, the QGP, is recreated by the LHC in CERN. When looking with the ALICE detector at these collisions the decay particles from those collisions are measured. By obtaining parameters from the invariant mass distributions (Gaussians) for neutral mesons π^0 and η the parameter fits of figures 8 and 9 were introduced. They work especially for π^0 nicely. The Gaussians that are created with these fits are mostly of the same form, since the values of the mean and sigma are close to the actual datapoints. When p_T gets larger, the difference between datapoint and fit also gets bigger, especially for η. Therefore the Gaussian with the highest p_T value is more different than the others. Then by analytically integrating the Gaussians, the raw yields are extracted. As can be seen for π^0 in figure 14 there is always ~ 2 percent deviation with respect to calculated value with numerical integration. The difference between the method with and without the constraint of the parameter fit is not very large. For η the deviation is around 25 percent (see figure 15). This was expected, since extracting the raw yield for η is much harder than for π^0. This results in a bigger deviation.
The RMS values for π^0 show that the uncertainty did not get smaller by using the analytically integrated yields. Nevertheless the values do come closer to reality, since different methods are being used to describe the same phenomenon and most of the times their values are alike. For η the difference between including or excluding the analytically integrated yields is larger than for π^0. Most of the time the RMS value is higher than the old one, which means the deviation is probably underestimated. But also for these results, the RMS does come closer to reality.
From now on this method can be used as an extra way to calculate the raw yield of neutral mesons, since it decreases the deviation of the raw yield extraction and gives a more realistic view at the RMS value.

References

[1] CERN Document Server (July 13th 2012), Experiments. Available at: http://cds.cern.ch/record/1997374 [Accessed May 30th 2018]

[2] Picture (February 1st 2012) available at: http://cds.cern.ch/record/1436153?ln=it [Accessed at May 30th 2018]

[3] Britt Griswold (December 21th 2012), NASA, How old is the universe?. Available at: https://map.gsfc.nasa.gov/universe/uni_age.html[Accessed May 8th 2018]

[4] Griffiths D. (2008), Introduction to Elementary Particles, Second Revised Edition, Wiley-VCH, Chapter 2, page 71.

[5] CERN Document Server (July 18th 2012), Heavy Ions and Quark Gluon Plasma. Available at: http://cds.cern.ch/record/1997370

[6] Griffiths D. (2008), Introduction to Elementary Particles, Second Revised Edition, Wiley-VCH, Chapter 3.

[7] CERN (February 8th 2012), ALICE (A Large Ion Collider Experiment). Available at: Cern Document Server, http://cds.cern.ch/record/1997265 [Accessed May 1st 2018]

[8] CERN, The ALICE Detectors. Available at: http://alice.web.cern.ch/ [Accessed May 8th 2018]

[9] CERN, More details on the ALICE ITS. Available at: http://alice.web.cern.ch/detectors/more-details-alice-its [Accessed May 8th 2018]

[10] Christakoglou P. (2017), Interaction of Particles with Matter, Reading material. Available at: https://pchrist.web.cern.ch/pchrist/Teaching.html [Accessed May 13th 2018]

[11] CERN, More details on the ALICE TPC. Available at: http://alice.web.cern.ch/detectors/more-details-alice-tpc [Accessed May 13th 2018]

[12] CERN, More details on the ALICE EMCal. Available at: http://alice.web.cern.ch/detectors/more-details-emcal [Accessed May 13th 2018]

[13] Sas M. (2016), Neutral Mesons and Direct Photon Flow, Masterthesis. Available at: https://dspace.library.uu.nl/handle/1874/337631 [Accessed Apr. 23rd 2018].

[14] Sas M., Bock F., Mühlheim D. (2015), Neutral meson measurements with EMCal-EMCal in ALICE in Pb-Pb collisions at $\sqrt{s} = 5.023$ TeV, Analysis Note.

[15] Koch K. (2011), Measurement of $\pi 0$ and η mesons with photon conversions in alice in proton-proton collisions at $\sqrt{s} = 0.9$, 2.76, 7 tev, PhD thesis, University of Heidelberg. Available at: http://www.ub.uni-heidelberg.de/archiv/13113 [Accessed at May 25th]

[16] Weisstein, Eric W., Root-Mean-Square, From MathWorld–A Wolfram Web Resource. Available at: http://mathworld.wolfram.com/Root-Mean-Square.html [Accessed at May 28th 2018]

Appendix A Invariant mass distribution fits

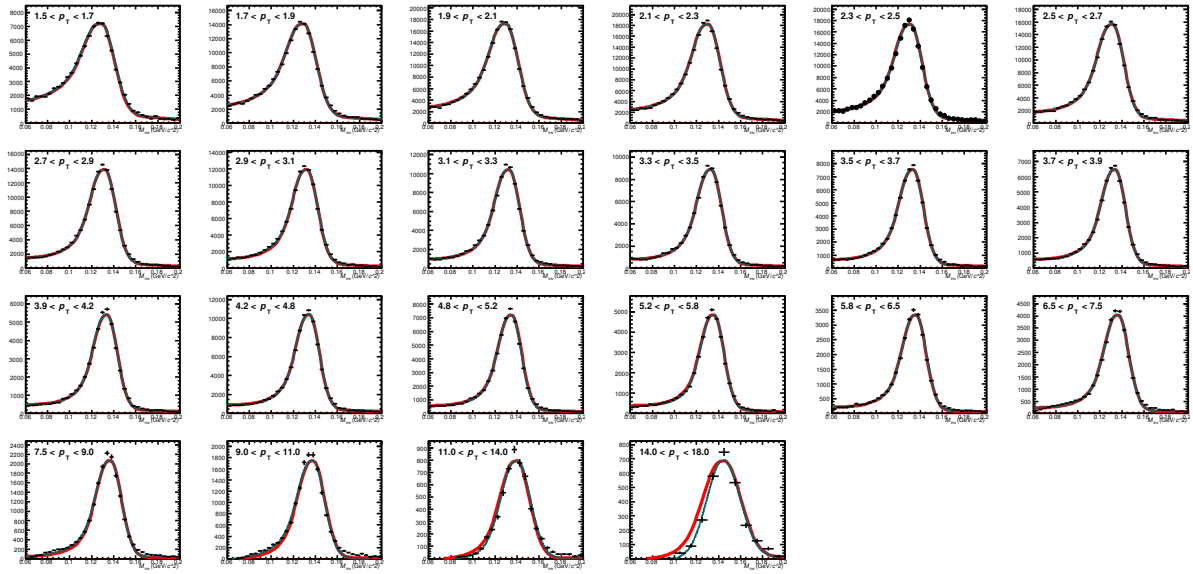

Figure 20: The fitted Gaussians through the datapoints for π^0. The red lines are the new Gaussian functions with the fitted parameters. The blue lines are the old Gaussians.

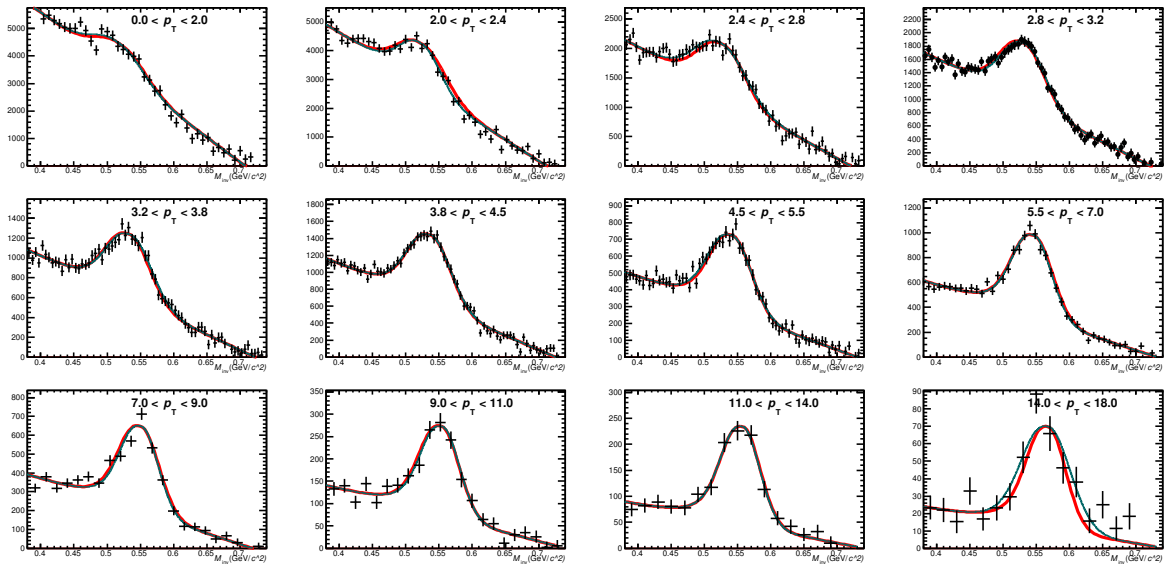

Figure 21: The fitted Gaussians through the datapoints for η. The red lines are the new Gaussian functions with the fitted parameters. The blue lines are the old Gaussians.